CGMM: Non-Invasive Continuous Glucose Monitoring in Wearables Using Metasurfaces

Hao Pan
Microsoft Research Asia (Shanghai)
panhao@microsoft.com

Yezhou Wang*
Shanghai Jiao Tong University
yezhouwang@sjtu.edu.cn

Jiting Liu*
Hong Kong University of Science and Technology
jitingliu@ust.hk

Ruichun Ma*
Microsoft Research Asia (Vancouver)
ruichunma@microsoft.com

Lili Qiu†
Microsoft Research Asia (Shanghai), UT Austin
liliqiu@microsoft.com

Yi-Chao Chen
Shanghai Jiao Tong University
yichao@sjtu.edu.cn

Guangtao Xue
Shanghai Jiao Tong University
gt_xue@sjtu.edu.cn

Ju Ren†
Tsinghua University
renju@tsinghua.edu.cn

ABSTRACT

Non-invasive continuous glucose monitoring for diabetes patients remains challenging despite ongoing interest. This paper presents CGMM, a novel non-invasive wireless glucose monitoring system integrated into wearable devices. It features a specially designed metasurface that couples with the wearable's antenna and tissue fluid beneath the skin, amplifying frequency response changes caused by subtle glucose concentration variations. To address individual tissue variability and optimize the passive metasurface design, we develop a tunable metasurface and a one-shot calibration method to obtain the impedance for optimal resonance in glucose sensing environments with unknown parameters. The calibrated impedance is then used for the inverse design and fabrication of an economical passive metasurface. We implement prototypes of CGMM and conduct extensive experimental evaluations. In human experiments involving ten participants using the prototype with LibreVNA, the overall performance is quantified with relative errors ranging from -5.02% to 6.93% and an RMSE of 9.65 mg/dL.

CCS CONCEPTS

• **Applied computing** → **Consumer health**; **Health informatics**; • **Human-centered computing** → *Mobile devices*.

KEYWORDS

Glucose sensing; Metasurface; Wearables

ACM Reference Format:
Hao Pan, Yezhou Wang, Jiting Liu, Ruichun Ma, Lili Qiu, Yi-Chao Chen, Guangtao Xue, and Ju Ren. 2025. CGMM: Non-Invasive Continuous Glucose Monitoring in Wearables Using Metasurfaces. In *The 31st Annual International Conference on Mobile Computing and Networking (ACM MobiCom '25), November 3–7, 2025, Hong Kong, Hong Kong.* ACM, New York, NY, USA, 16 pages. https://doi.org/10.1145/3680207.3723474

1 INTRODUCTION

Diabetes is a prevalent chronic disease with significant impacts on the individuals' quality of life [2]. Continuous glucose monitoring (CGM) remains vital for patients to understand their condition, prevent hypoglycemic or hyperglycemic events, and evaluate medication effectiveness [5, 6, 46]. Common techniques use electrochemical methods to convert glucose concentration into electrical signals [60]. However, these require invasive procedures skin-pricks [8], causing pain, inconvenience, and potential infection.

Non-invasive glucose monitoring using spectroscopy has been validated in prototypes and theory, as glucose exhibits characteristic absorption peaks in the infrared spectrum. Although companies like Samsung and Apple have launched smartwatches, these devices have not yet achieved this capability [11, 24, 45]. Spectroscopy-based technology faces numerous challenges, such as being highly sensitive to noise and susceptible to ambient light interference, necessitating the use of complex black boxes to mitigate these effects [39, 76]. Additionally, it is affected by factors like skin tone [72]. Glucose molecules affect not only the optical spectrum but also

*Yezhou Wang, Jiting Liu, and Ruichun Ma did this work as interns at Microsoft Research Asia
†Ju Ren and Lili Qiu are the corresponding authors.

ACM MobiCom '25, November 3–7, 2025, Hong Kong, Hong Kong

ACM ISBN 979-8-4007-1129-9/25/11
https://doi.org/10.1145/3680207.3723474

the dielectric spectrum [67]. Changes in glucose levels can alter the permittivity of blood and surrounding tissue fluid, also known as interstitial fluid (ISF), which affects the propagation of electromagnetic (EM) waves. This provides a theoretical basis for using wireless signals to monitor blood glucose levels. Therefore, we are exploring the electrophysical properties of glucose to advance the development of non-invasive blood glucose measurement in wearable devices. Our goal is to leverage existing wireless frequency resources, such as Wi-Fi or Ultra-Wideband (UWB), to develop a cost-effective, non-invasive, and easily deployable CGM solution.

Variations in glucose concentration, such as a change of 100 mg/dL, have minimal effects on the permittivity of blood and tissue fluid. In the Wi-Fi and UWB bands, each 100 mg/dL change in glucose concentration results in less than a 0.001 dB change in amplitude and a 0.01° change in phase of the antenna's reflected frequency response. Recent research in wireless liquid sensing typically requires containers of sufficient size and/or thickness to detect propagation feature changes [14, 19, 61]. Other studies use RFID tags to identify liquid types but do not offer fine-grained concentration sensing [27, 70]. Therefore, inferring glucose levels using wireless signals presents a significant challenge. This motivates us to develop a system that can "amplify" changes in wireless signal frequency responses using metasurfaces.

In this paper, we propose an innovative non-invasive CGM method called CGMM. As shown in Figure 1, we place the designed passive metasurface behind a wearable device on the user's arm or wrist. A metasurface can couple with the underlying tissues, such as fat and muscle, converting subtle changes in glucose concentration in the tissue fluid into detectable changes in the antenna's reflected frequency response. Compared to transmission response, we choose reflection response because it only requires equipment deployment on one side and can even be implemented with a single antenna.

The essence of CGMM is to design and optimize a metasurface that is highly sensitive to the subtle permittivity variations in tissues caused by glucose changes. Our optimized metasurface should achieve strong resonance with the human tissues. At this resonant frequency, due to impedance matching by the metasurface, EM waves can propagate efficiently with minimal reflection. Consequently, subtle permittivity changes caused by glucose concentration variations can lead to shifts in the resonant frequency. Designing such a metasurface requires an accurate optimization model that includes the user's detailed tissue parameters, such as thickness and permittivity of each tissue layer. However, obtaining the thickness by imaging techniques (such as X-rays and MRI) and measuring permittivity through electrophysical methods are cumbersome and even somewhat impractical for the users. Therefore, optimizing a passive metasurface in environments with unknown parameters is highly challenging.

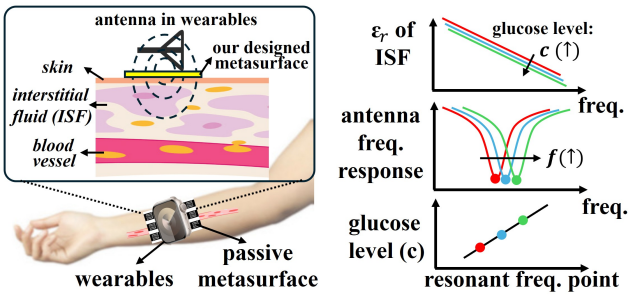

Figure 1: CGMM enables the continuous monitoring of glucose changes by utilizing the frequency response of wearable antennas

To address this challenge, we propose a one-shot calibration process to optimize the passive metasurface. Specifically, we design a tunable metasurface and adjust variable capacitors to optimize resonance between the metasurface and human tissues with uncertain parameters. Each user requires the tunable metasurface only once for calibration, after which it can be converted into a personalized passive metasurface. We use a lumped element planar capacitor template to design the passive metasurface, ensuring the metasurface units are much smaller than half the wavelength at the operating frequency. This is crucial since antennas in wearable devices usually operate below 10 GHz. In our study, the metasurface units measure 5 mm×5 mm. Arranged periodically, the final metasurface can fit various small wearable devices, such as 4 cm×4 cm smartwatches. Our final system employs passive metasurfaces that do not require batteries or additional circuits, allowing for easy plug-and-play deployment.

We fabricate a tunable metasurface prototype for one-time calibration and design various experimental scenarios with unknown parameters to evaluate CGMM. In each experiment, we use the tunable metasurface to obtain calibration impedance parameters and then create corresponding passive metasurfaces for testing glucose estimation performance. We use the FreeStyle Libre CGM sensor [41] to obtain accurate glucose concentrations in the tissue fluid. A radio measurement device, specifically a portable Vector Network Analyzer (VNA) or a portable Software-Defined Radio (SDR), is used to measure the antenna's reflected frequency response. We conduct human trials involving ten volunteers who consume high-sugar beverages or foods to alter their blood glucose levels. Both the CGMM prototypes and CGM sensors are attached to the volunteers' arms to measure tissue fluid glucose changes over three hours. The experimental results indicate that our proposed system has an RMSE of approximately 9.65 mg/dL using the prototype with LibreVNA. To demonstrate the scalability and plug-and-play nature of our designed metasurface, we attach the metasurface to the RX antenna of a commercial UWB radar module, *i.e.*, SLMX4 [58], thereby converting it into a CGMM prototype. We validate its glucose

estimation performance and obtain an RMSE of 20.53 mg/dL; the experimental results are also promising.

Our major contributions are as follows:

- To the best of our knowledge, CGMM is the first system to enable non-invasive continuous glucose monitoring in wearables using metasurface technology.
- Our proposed CGMM features an optimized passive metasurface that amplifies subtle glucose concentration changes into detectable variations in the reflection frequency response of the wearable antenna.
- We propose a tunable metasurface for one-shot calibration to address the issue of unknown human tissue parameters. The calibrated impedance parameters guide the development of a personalized passive metasurface.
- In IRB-approved human trials, our system achieves an average glucose sensing error of 9.65 mg/dL with a prototype featuring an external antenna and LibreVNA, and 20.53 mg/dL with a prototype using our metasurface with a commercial UWB radar device.

2 RELATED WORK

2.1 Glucose Sensing Methods

2.1.1 Invasive glucose sensing. Invasive glucose monitoring methods, such as fingerstick blood sampling [37] and subcutaneous implantation [32], rely on electrochemistry principles to detect blood glucose levels. Most glucometers use oxidase to react with glucose molecules in blood samples, converting glucose concentrations into electrical signals [30]. Continuous glucose monitoring products use implanted sensors with oxidase in subcutaneous tissue fluid [50], reducing the need for finger pricks. However, this method is costly and powered, as the sensors need to be replaced every two weeks, and may also cause skin irritation [1]. The academic community has extensively researched implantable blood glucose sensors based on EM resonance properties [9, 17, 38]. Nevertheless, these methods require sensor implantation, which can also lead to discomfort and increased costs.

2.1.2 Non-invasive glucose sensing. **Spectroscopy based methods:** Glucose molecules can absorb spectra at specific frequency ranges due to their characteristic vibration and rotation modes [47, 71]. Relevant researches and commercial products measure blood glucose levels by transmitting lasers into subcutaneous tissue and analyzing the capillary spectrum [4, 12, 39, 48, 76]. These methods commonly use a black box to enclose testing components and body parts, like fingers, to block ambient light interference. Consequently, current spectroscopic methods are limited to snapshot measurements because these bulky boxes are difficult to incorporate into wearable devices and continuous monitoring systems. Additionally, optical-based sensing methods are also sensitive to

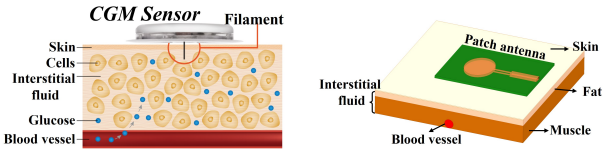

(a) Working principle of CGM [8] (b) Using antenna to sense glucose

Figure 2: Left is an invasive CGM sensor; right is a non-invasive setup using an antenna to measure glucose changes in tissue fluid

the skin characteristics [72]. Some researches and the existing commercial wearable products utilize PPG signals combined with machine learning algorithms for blood glucose monitoring [13, 15, 34, 55, 75]. PPG infers blood glucose levels indirectly through changes in blood flow rather than measuring glucose molecules directly. PPG signals are affected by factors like blood flow, vascular condition, heart rate, and external interference, resulting in no direct correlation with blood glucose concentration. This limits the accuracy and reliability of using PPG alone for glucose measurement [42]. Thus, even with advanced signal processing and deep learning algorithms, it is still challenging to accurately obtain glucose concentrations from PPG [7, 18].

Dielectric spectrum based methods: Glucose variations alter the permittivity of the blood and tissue fluid, allowing estimation of glucose concentration through analysis of EM signal characteristics (*e.g.*, attenuation, phase changes) [31]. Compared with spectroscopy, dielectric spectrum can be obtained using existing radio frequency (RF) resources (*e.g.*, Wi-Fi and UWB) in wearable and mobile devices. But the RF hardware on wearables and mobile devices cannot capture these particularly small changes in EM signals. Some commercial products utilize the customized hardware to measure dielectric spectrum changes, *i.e.*, EM signal attenuation, in the fingertip or earlobe for glucose monitoring. However, these products are costly (*e.g.*, GlucoTrack costs $2,120 [35]). Some research utilizes dielectric spectrum sensing to monitor glucose levels. [29, 52] design wearable EM resonant sensors placed near the arm or lower leg for blood glucose monitoring. However, these designs require deploying cables and antennas of half-wavelength size (*e.g.*,~6 cm at 2.4 GHz), which is impractical for users. Omer *et al.* propose a mmWave blood glucose detection system using the Soli mmWave Radar board to sense glucose in a test tube at 100 mg/dL intervals [51, 59]. This system analyzes reflected signals for concentration classification using machine learning, making it highly sensitive to the environment. Metasurface is a 2D EM metamaterial [43, 44, 53, 64, 68], Jun *et al.* explore terahertz and metasurface-based glucose sensing but provide only simulation results without developing an actual system for validation [73]. Other researchers use sub-terahertz radiation

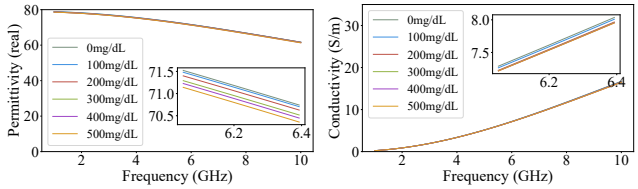

Figure 3: Permittivity values of glucose solutions at different glucose concentrations with a background of pure water. These data are fitted using the single pole Cole-Cole model and the measured data from [67]

(near 0.1 THz) for glucose solution reflectance measurement [63, 66, 73]. However, THz and sub-THz devices are costly and not available on mobile devices.

Our work: Our proposed CGMM is non-invasive and lies in the careful design of the metasurface. We provide a demonstration of the feasibility of noninvasive blood glucose measurement in wearable scenarios by utilizing RF channels and metasurface technology.

2.2 Liquid Sensing with RF Signals

Several studies have leveraged the propagation characteristics of wireless signals in liquids to estimate their type and concentration. Ashutosh *et al.* develop LiquID [14], a low-cost liquid recognition system based on the relationship between the attenuation factor and the dielectric constant, using UWB antennas. WiMi [19] and LiqRay [61] can identify liquid type and concentration using Wi-Fi signals, respectively. However, these systems are impractical for glucose monitoring because of their specific requirements related to container size or liquid thickness. Unsoo *et al.* propose RF-EATS [27, 28], a method that involves placing RFID tags on the surface of liquid containers and analyzing the spectral features of the reflected signals. Binbin *et al.* develop a liquid classification system using RFID [70]. However, these methods cannot differentiate liquid concentrations with the fine granularity required for glucose monitoring, nor have they verified feasibility in human experiments. Also as shown in Figure 14, our preliminary analysis demonstrates that antennas alone are not sufficiently sensitive for glucose sensing. This is because antennas on existing commercial devices are usually optimized for wireless communication and radar applications, lacking the impedance matching and fine-grained glucose sensing capabilities.

3 PRELIMINARY ANALYSIS

Our goal is to develop a non-invasive CGM system. As shown in Figure 2(b), we aim to use antennas in wearable devices to detect the subtle changes of glucose concentration, thus replacing traditional invasive CGM sensors. In this section, we explore the impact of glucose concentration changes on the permittivity values of human tissue fluid. We then discuss

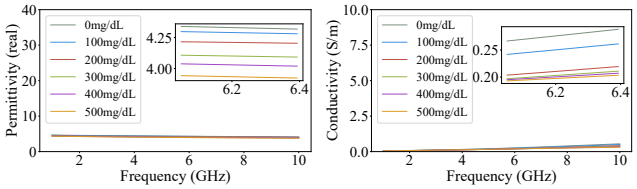

(a) Fat tissue fluid at different glucose levels

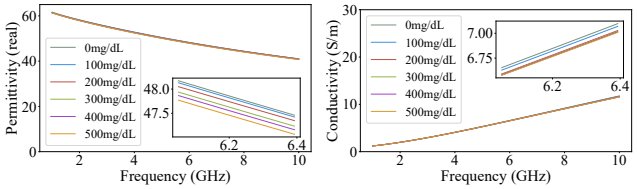

(b) Muscle tissue fluid at different glucose levels

Figure 4: Examples of permittivity values of fat and muscle tissue fluid, with varying glucose concentrations. These data are fitted using the Cole-Cole model

the challenges of directly measuring glucose concentration changes in tissue fluid with Wi-Fi antennas.

3.1 Permittivity of Human Tissues versus Glucose Concentration

Characterization of the permittivity of human tissue fluid at different glucose levels is the theoretical core of glucose sensing based on radio frequency signals. Permittivity, often represented by the relative permittivity ϵ_r, is the ratio of absolute permittivity ϵ to vacuum permittivity ϵ_0 and can be expressed as a complex function: $\epsilon_r(\omega) = \epsilon_r'(\omega) - j\epsilon_r''(\omega)$, where ω is the angular frequency, and ϵ_r' and ϵ_r'' are the real part and the imaginary part, respectively. The Cole-Cole model effectively captures frequency-dependent permittivity behavior, which allows us to fit relative permittivity properties using finite measured values at a few frequencies. The model [36] captures complex permittivity as follows:

$$\epsilon_r = \epsilon_\infty + \sum_{i=1}^{n} \frac{\epsilon_s - \epsilon_\infty}{1 + (j\omega\tau_n)^{1-\alpha_n}} + \frac{\sigma_i}{j\omega\epsilon_0'} \tag{1}$$

where ϵ_s and ϵ_∞ represent the limits of permittivity at low and high frequencies, ϵ_0 is the free space permittivity, τ denotes relaxation time, α describes relaxation loss peak broadening, and σ_i is ionic conductivity [25]. Here, we set n=1 and α=0 (*i.e.*, the single pole Cole-Cole model) and fit the model parameters of the glucose solutions (with pure water as the background), as shown in Table 1 in the appendix. The frequency-dependent complex permittivity curves for various glucose concentrations is depicted in Figure 3.

The intercellular spaces in these tissues are filled with interstitial fluid. When blood glucose concentration changes, due to osmotic pressure, glucose molecules permeate from the

blood vessels into the interstitial fluid, causing corresponding changes in the glucose concentration of the interstitial fluid. However, the glucose-dependent permittivity changes of human tissue fluid at different glucose levels have not been thoroughly investigated. To address this, we model the tissue fluid as a mixture of tissue and glucose liquid. Using the Maxwell Garnett formula [69], we assume that the tissue fluid within various biological tissues serves as the background medium and glucose acts as the dispersed phase, the mixture's permittivity can be characterized as a two-phase composite system:

$$\epsilon_{eff} = \epsilon_{ts} + 3c_{glu}\epsilon_{ts}\frac{\epsilon_{glu} - \epsilon_{ts}}{\epsilon_{glu} + 2\epsilon_{ts} - c_{glu}(\epsilon_{glu} - \epsilon_{ts})} \quad (2)$$

where ϵ_{eff} represents the effective permittivity of the mixture, ϵ_{ts} is the complex permittivity of the biological tissue, and ϵ_{glu} is the permittivity of the glucose solution with a volume fraction c_{glu}. Since glucose concentration is low ($c_{glu} \ll 1$), Eq. 2 can be simplified as [26]:

$$\epsilon_{eff} = \epsilon_{ts} + 3c_{glu}\epsilon_{ts}\frac{\epsilon_{glu} - \epsilon_{ts}}{\epsilon_{glu} + 2\epsilon_{ts}} \quad (3)$$

We consider the mainly two types of biological tissues, fat and muscle, whose complex permittivity values are obtained from [23, 57]. Here, we simplify the model by using the permittivity of tissue fluid in place of that of biological tissue.

To determine the effective permittivity of fat and muscle tissues mixed with glucose, we first need to know the permittivity of pure glucose. The permittivity of pure glucose can be approximated by applying the Maxwell Garnett model to glucose-water mixtures. The effective permittivity of glucose-water solutions $\epsilon_{eff-gluwater}$ at known concentrations can be modeled by the single pole Cole-Cole model with parameters listed in Table 1. Therefore, the permittivity of pure glucose can then be expressed as:

$$\epsilon_{glu} = -\frac{2(\epsilon_{eff-gluwater} - \epsilon_{wat}) + 3c_{glu}\epsilon_{wat}}{\epsilon_{eff-gluwater} - \epsilon_{wat} - 3c_{glu}\epsilon_{wat}}\epsilon_{wat} \quad (4)$$

Once the complex permittivity of pure glucose ϵ_{glu} is established, it can be used in conjunction with the Eq. 3 to calculate the glucose-dependent permittivity of fat and muscle tissues. These properties are then fitted using a double Cole-Cole model ($n = 2$), with the resulting parameters listed in Table 2 and 3, respectively. The fitted frequency-dependent permittivity curves of the ISF, *i.e.*, fat and muscle, are shown in Figure 4(a) and (b), respectively. From the simulated results, varying glucose concentrations have a minimal impact on the permittivity of the tissues. When the glucose concentration changes from 0 to 500 mg/dL, the real part of the relative permittivity decreases by less than 0.3 for fat and less than 0.5 for muscle. Concurrently, the imaginary part increases by less than 0.05 for both fat and muscle.

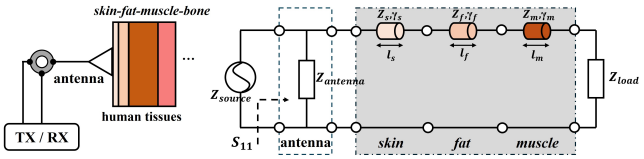

Figure 5: Equivalent circuit model of using antenna to sense concentration level in tissue fluid

3.2 Impact of Glucose Concentration Changes on Wireless Signals

We next theoretically analyze the impact of varying glucose concentrations on the permittivity of human tissues and its effects on propagation of EM waves. To this end, we utilize equivalent circuit theory to model the setup depicted in Figure 2(b), and the circuit model is shown in Figure 5. We can derive the reflection ratio from the equivalent circuit by calculating the ABCD matrix [54]. The ABCD matrix is a 2×2 matrix used to characterize the properties of linear two-port networks in electrical circuits. The elements A, B, C, and D can be calculated to describe the transmission characteristics.

We model the antenna as a parallel impedance, denoted as $Z_{antenna}$. And the ABCD matrix of the antenna is: $M_{antenna} = \begin{bmatrix} 1 & 0 \\ \frac{1}{Z_{antenna}} & 1 \end{bmatrix}$. When EM waves are radiated from the antenna, they undergo reflection, transmission, and absorption through the skin, fat, and muscle tissues. We model the tissue layers as transmission lines [54], which involve parameters l for thickness, Z for complex characteristic impedance, and γ for propagation constant. Both Z and γ are derived from relative permittivity ϵ_r and relative permeability μ_r as follows: $Z = \sqrt{\frac{\mu_0\mu_r}{\epsilon_0\epsilon_r}} = Z_0\sqrt{\frac{\mu_r}{\epsilon_r}}$ and $\gamma = \frac{j\omega\mu_0\sqrt{\mu_r\epsilon_r}}{Z_0} = \gamma_0\sqrt{\mu_r\epsilon_r}$, where Z_0 is free space's characteristic impedance (377 Ω), γ_0 is free space's propagation constant (*i.e.*, $\frac{j\omega}{c}$), and c is the speed of light. Since human tissues are not magnetic materials, we set the relative permeability μ_r of each tissue to 1. The corresponding ABCD matrix of the transmission line is as follows:

$$M_{tl} = \begin{bmatrix} cosh(\gamma l) & Zsinh(\gamma l) \\ \frac{sinh(\gamma l)}{Z} & cosh(\gamma l) \end{bmatrix} \quad (5)$$

Thus, based on the equivalent circuit of Figure 5, we can create an overall ABCD matrix to characterize this circuit:

$$M_{total} = M_{antenna}M_{tl-skin}M_{tl-fat}M_{tl-muscle} = \begin{bmatrix} A & B \\ C & D \end{bmatrix} \quad (6)$$

We can then convert the ABCD matrix to S-parameters to derive the S_{11} (*i.e.*, reflection ratio) of this circuit:

$$S_{11} = \frac{A + B/Z_{load} - CZ_{source} - D}{A + B/Z_{load} + CZ_{source} + D} \quad (7)$$

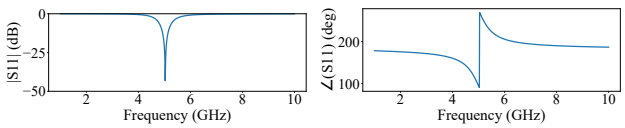

(a) Antenna@5GHz frequency response

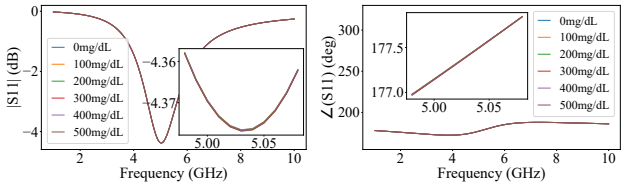

(b) Antenna attached to the human tissues

Figure 6: Effect of glucose concentration changes in the human tissues on the antenna's S_{11} parameters

where Z_{source} and Z_{load} are the characteristic impedance of the excitation source and the load, respectively. Here, we set Z_{source} to 50 Ω, and use the bone as the load of this circuit. $Z_{load} = Z_{bone} = \frac{Z_0}{\epsilon_{r-bone}}$ [21].

Assume a scenario where a Wi-Fi antenna is used to sense glucose changes in tissue fluid. For an antenna operating at 5 GHz, modeled as a parallel LC circuit with inductance L = 1 nH and capacitance C = 0.1 pF, the impedance can be expressed as: $Z_{antenna} = \frac{\omega L}{(\omega^2 LC-1)j}$. Figure 6(a) show the resonance of this antenna in the air, represented by the S_{11} parameters. We set the thicknesses of the skin, fat, and muscle layers to 1 mm, 10 mm, and 30 mm, respectively. The permittivity values of the skin and bone are defined as specified in [21]. The permittivity parameters of fat and muscle across varying glucose levels are set as shown in Figure 4(a) and (b). After placing the antenna on the user's tissue, the S_{11} parameters across different glucose concentrations are illustrated in Figure 6(b). We observe the following: (1) The antenna's resonance is significantly attenuated due to impedance mismatch, resulting in most EM waves not effectively propagating to human tissue; (2) Although glucose concentration changes alter the permittivity of human tissues, this change is hardly reflected in the antenna's S_{11}. Here, we use a Wi-Fi antenna as an example. However, antennas operating at other frequency bands like UWB and millimeter waves face similar challenges. This is due to similar principles of the antenna design and minimal changes in glucose permittivity across frequencies.

4 CGMM SYSTEM DESIGN

4.1 Overview of CGMM

In this paper, we propose the CGMM system, which introduces an optimized metasurface between the antenna and the user's tissue to amplify the changes in the antenna's reflection frequency response caused by variations in glucose concentration. Figure 7 provides an overview of CGMM. Initially, we establish an equivalent circuit model (see Figure 7(a)) to describe the frequency response of the antenna to the glucose concentration changes in the tissue fluid after incorporating the metasurface. Considering the variability of parameters in human tissues, such as the thickness and permittivity of skin, fat, and muscle, we introduce a novel calibration step by designing a tunable active metasurface, as depicted on the left side of Figure 7(b). We define the parameter space range related to human tissue characteristics and determine the tunable impedance range for calibration. The right of Figure 7(b) shows the calibration step, where we identify the optimal impedance of the tunable metasurface for a target user to achieve the best coupling resonance. Finally, as shown in Figure 7(c) and (d), we facilitate the design of the final passive metasurface through the calibrated impedance and the equivalent ABCD matrix. The optimized passive metasurface will work in conjunction with the specified antenna to achieve high-quality resonance with the tissues of the user's arm.

4.2 Modeling Metasurface-aided Glucose Concentration Sensing

4.2.1 Metasurface Modeling. A metasurface is a 2D material with negligible thickness, typically composed of a metal layer and a substrate layer. The metal layer plays a crucial role by generating surface currents and magnetic currents when excited by incident EM waves, thereby enabling the control of the propagation of incident EM waves by producing new EM waves. The substrate primarily serves to support the metal layer. In the equivalent circuit theory, modeling the metasurface is depicted in Figure 7(a). The metal layer is modeled as a parallel component, and its equivalent impedance is denoted as Z_{metal}, the corresponding ABCD matrix is expressed as $M_{metal} = \begin{bmatrix} 1 & 0 \\ \frac{1}{Z_{metal}} & 1 \end{bmatrix}$. Here, we neglect the resistance of the metal layer, so its impedance is purely imaginary, such as jX. The substrate layer is modeled as a transmission line. Assuming the propagation constant and characteristic impedance of the substrate material are γ_d and Z_d, thickness of it is l, its ABCD matrix is represented as $M_{tl-mts} = \begin{bmatrix} cosh(\gamma_d l_d) & Z_d sinh(\gamma_d l_d) \\ \frac{sinh(\gamma_d l_d)}{Z_d} & cosh(\gamma_d l_d) \end{bmatrix}$. Consequently, the overall ABCD matrix of the metasurface can be formulated as $M_{mts} = M_{metal} M_{tl-mts}$.

4.2.2 Optimization Objective. Our optimization objective is to seek the optimal metasurface design such that the antenna's reflection coefficient S_{11} exhibits the maximum change when there is a variation in the glucose levels in the tissue fluid. To achieve this, we first establish a comprehensive circuit model based on the metasurface for sensing glucose variations in the tissue fluid, also as shown in Figure 7(a), and

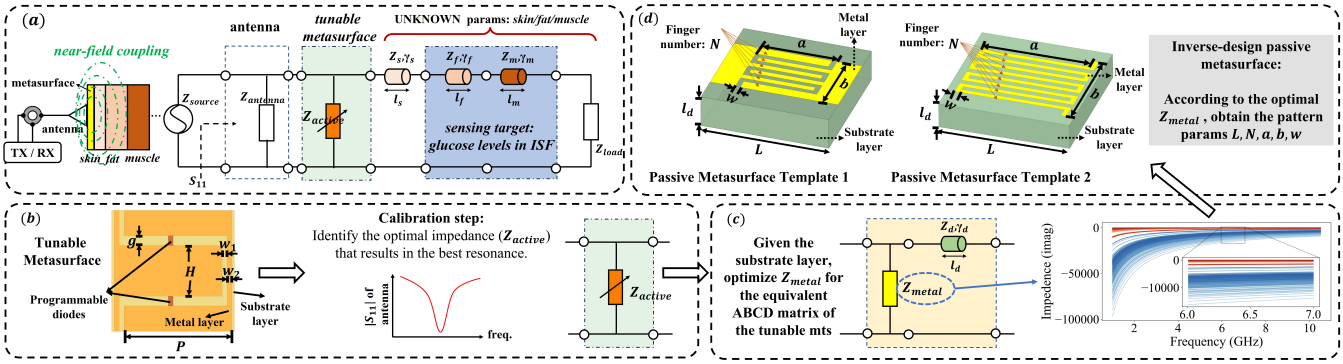

Figure 7: Pipeline for optimizing the glucose-sensitive passive metasurface: (a) We introduce a metasurface and establish an equivalent circuit model to describe the antenna's frequency response. (b) To address unknown human tissue parameters, we design a tunable metasurface for calibration. (c) The equivalent impedance from the calibrated tunable metasurface is used to optimize passive metasurface design. (d) We pre-design two template-based passive metasurfaces and use equivalent impedance to inversely solve the geometric parameters. Note that the curves in (c) show impedance values for different geometric parameters, with red curves for Template 1 and blue for Template 2

construct the ABCD matrix for the entire system as follows:

$$M_{total} = M_{antenna}\underline{M_{metal}}M_{tl-mts}M_{tl-skin}M_{tl-fat}M_{tl-muscle} \tag{8}$$

According to Eq. 7, we can obtain the S_{11} parameters. Considering that the substrate material does not exhibit capacitive or inductive characteristics, generally, when designing a metasurface, the primary optimization focuses on the pattern of the metal layer to achieve the desired impedance characteristics.

During the optimization process, we first select the substrate material type and its thickness. We also define the operational frequency band in advance, such as Wi-Fi (5-6 GHz) or UWB (7-10 GHz). This allows us to optimize the metasurface to function effectively within the wireless frequency bands supported by wearable devices. Therefore, the definition of our optimization objective is as follows:

$$\max_{Z_{metal}} \sum_{i=1}^{m}\sum_{j=1,j\neq i}^{m} ||S_{11}(c_i) - S_{11}(c_j)||^2 \tag{9}$$

where m denotes the glucose level number, and c_i is the $i-th$ glucose concentration value. For example, $[c_0, c_1, c_2, \ldots, c_5] = [0, 100, 200, \ldots, 500]$ mg/dL. $S_{11}(c_i)$ means the S_{11} parameters of the glucose solution with concentration c_i. The optimization goal is to maximize the Euclidean distances of the S_{11} parameters across different glucose concentrations. We use this metric for two reasons: (1) Maximizing the distances in the frequency response increases the differences to make subsequent glucose level identification easier, (2) Compared to $min(\cdot)$ and $argmin(\cdot)$ functions, the distance-based loss function has a gradient during backpropagation, which supports gradient descent optimizer.

4.2.3 Validation of Optimization Results. To validate our concept of designing the metasurface to reflect subtle changes in glucose concentration in tissue fluid through detectable antenna's S_{11} variations, we assume specific scenarios and assess the feasibility of the proposed optimization model. In details, we assume that the permittivity values of the user's various tissues is known and consistent with the parameters outlined in Sec. 3.2. We set the substrate material of the metasurface to FR4 with a thickness of 1.2 mm.

We design antennas and metasurfaces to operate effectively in two target frequency bands: 5-6 GHz and 7-8 GHz. We use equivalent parallel LC circuits to model. The parameters for the antenna at 5.5 GHz are: $L = 1.45\ nH$ and $C = 0.53\ pF$, and the parameters for 7.5 GHz are: $L = 1.06\ nH$ and $C = 0.27\ pF$. We optimize the equivalent impedance, *i.e.*, jX, of the metasurface's metal layer to ensure compatibility with each antenna's operational frequency. The optimization results are presented in Figure 8.

Our findings show that the optimized metasurface effectively reflects tissue fluid glucose changes through S_{11} parameters and operates well within specified frequency bands. Simulations indicate that glucose variations cause resonance point frequency shifts, with about ~40 MHz per 100 mg/dL change. While amplitude and phase at the resonance point are affected, the link between glucose concentration and frequency shift is more consistent. Additionally, measuring power is easier than phase for RF devices. Thus, we use resonance point shifts to detect glucose concentration changes.

4.3 Calibration with a Tunable Metasurface

A major challenge in practical use arises from the issue of the unknown parameters of a user's tissues. To address this issue, we propose an innovative one-shot calibration. This method utilizes a tunable metasurface with variable capacitors to achieve optimal impedance resonance with the target user's tissues. After obtaining the optimal resonance, we use HFSS to determine the equivalent impedance curve of the

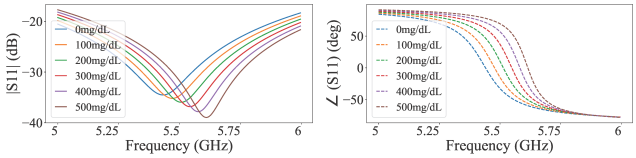

(a) Optimal metasurface operating at around 5-6 GHz

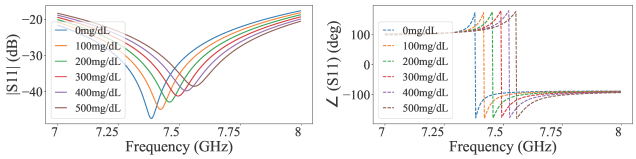

(b) Optimal metasurface operating at around 7-8 GHz

Figure 8: Reflected frequency responses of two different antennas on the glucose concentrations based on the optimized metasurface designs

tunable metasurface within the specific frequency band (*i.e.*, $Z_{a-mts}(\omega)$). Then we derive a passive metasurface with the equivalent ABCD matrix.

Note that we only need to handle unknown parameters of the user's tissues because the antenna parameters can be obtained, *e.g.*, by measuring the operational frequency bands and equivalent impedance of it using a VNA or through finite element simulation like HFSS [3].

4.3.1 Tunable Metasurface Design. The tunable metasurface is a crucial component of the calibration process and must be carefully designed for effective resonance coupling with the tissue layers on most users' arms by adjusting the variable capacitors. Figure 7(b) illustrates a tunable metasurface unit design, featuring two varactor diodes as programmable capacitors and a metallic patch acting as a mini antenna. It is essential to determine the specific geometric parameters of the tunable metasurface unit, as well as the tuning range of the adjustable capacitors. To achieve this, we define parameter ranges for each tissue layer. The thickness ranges are as follows: skin (0.5-2 mm), fat (1-10 mm), and muscle (10-30 mm). We utilize published permittivity data [21] and our fitted Cole-Cole model parameters (see Sec. 3.1) for glucose concentration changes in fat and muscle tissues.

We adopt the same optimization model as in Sec. 4.2 to solve for the design parameters of the tunable metasurface. First, we specify that the substrate material of the tunable metasurface is FPC with a thickness of 0.05 mm. Subsequently, we iterate over all possible tissue parameters. For each set of parameters, we optimize the impedance to achieve the best detectable differences in the S_{11} parameters, corresponding to changes in glucose concentration in the tissue fluid. Ultimately, we obtain a series of equivalent impedance parameters for the metal layer. We use the built-in optimizer of HFSS software to optimize the pattern set parameters and the impedance range of the varactor diode that satisfy the

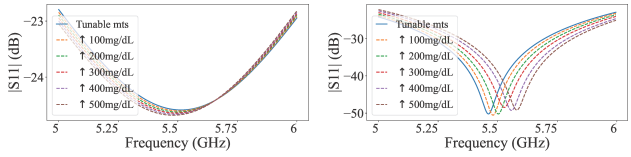

(a) Low Q factor (b) High Q factor

Figure 9: Enhancing resonant Q factor can amplify S_{11} variation in response to glucose concentration changes

aforementioned optimized impedance range, facilitating the selection of the varactor diode.

4.3.2 Calibration Process. For a measurement target with specified parameters, our calibration process is described below. We place the tunable metasurface between the antenna and the target environment (*e.g.*, skin on the arm). We then systematically vary the capacitance of the varactor diodes from a minimal to a maximal value. By observing the S_{11} parameter of the antenna, we identify the capacitance value that yields optimal resonance and the best Q factor under the current environmental setup. Once the optimal capacitance for resonance coupling is determined, we use HFSS simulation to derive the corresponding equivalent impedance. This information enables the optimization of a passive metasurface that matches the ABCD matrix of the tunable metasurface, ultimately facilitating a glucose-sensitive passive metasurface for unknown environmental conditions.

Note that we only need to tune the varactor diode once for the current glucose level to obtain the calibrated impedance. This is based on our empirical observation for passive metasurface design optimization results: an optimal resonance quality at one concentration suffices to optimize our objective in Eq. 9. $\frac{\partial|S_{11}|}{\partial f}|f_0$ is the derivative at the resonant frequency (f_0), reflecting the steepness of the resonance peak. We use the resonant Q factor, to capture the quality of a resonant system. $Q = \frac{f_r}{\Delta f}$, where f_r is the resonance frequency and Δf is the bandwidth, typically defined as the frequency range between the points on the response curve that are at the -3 dB level. A larger Q indicates a better resonant quality. As the Q factor increases, the absolute value of the derivative $\frac{\partial|S11|}{\partial f}|f_0$ also increases, because the resonance peak becomes sharper. Consequently, for a given perturbation in capacitance (ΔC, *e.g.*, 0.01 pF), the change in ($\Delta|S_{11}|$) will be more significant. Therefore, for an LC resonant circuit with a high Q factor, a small change in capacitance (*e.g.*, changes in glucose concentration) will induce a more pronounced change in (S_{11}) at the resonant frequency compared to a circuit with a lower Q factor. Figure 9 presents two cases wherein different metasurfaces are optimized for coupling with blood. It is evident that a higher resonant Q-factor results in a larger variation of the S_{11} parameter caused by changes in blood glucose concentration. This observation justifies our calibration process.

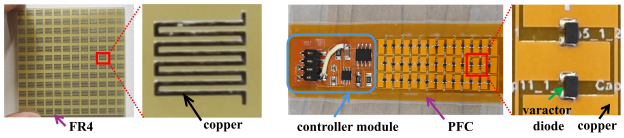

(a) Passive metasurface (b) Tunable metasurface

Figure 10: Examples of the fabricated metasurfaces, both the metasurface unit with 5 mm×5 mm

Under any glucose concentrations, calibration is achieved by simply identifying the parameters of the tunable metasurface that result in an optimal resonant coupling.

4.4 Inverse Design of Passive Metasurfaces with Calibrated Impedance

During the calibration process, we obtain the equivalent impedance value of the metal layer in the tunable metasurface, and the overall ABCD matrix is: $M_{t-mts} = M_{metal-t}M_{tl-t}$. To make the passive metasurface realize the same functionality as the calibrated active metasurface, we need to make their overall ABCD matrices the same in the operating frequency bands. We set the ABCD matrix of passive metasurface as $M_{p-mts} = M_{metal-p}M_{tl-p}$. By establishing an impedance function related to the geometric parameters of the metal layer, we can obtain the $Z_{metal-p} = jF_{tpl}(L, a, b, c, N)$, tpl is the template id (*i.e.*, 1 or 2), and the detailed curves of the impedance is shown in Figure 7(c). Consequently, it is essential to obtain the metal pattern's impedance function for various geometric parameters and establish a relationship between these parameters and the impedance function coefficients. The curves can be approximated by an n-order polynomial function, *i.e.*, $\chi(f) = \chi_1 f^n + \chi_2 f^{n-1} + ... + \chi_{n+1}$. For each χ_i coefficient, an equation incorporating geometric parameters is fitted, *i.e.*, $\chi_{tpl} = F_{tpl}(L, a, b, c, N)$. Along with the thickness l_d of the substrate FR4 layer, we can obtain the total ABCD matrix of the passive metasurface. Our objective is to match the equivalent impedance of the passive metasurface with that of the calibrated one so that their ABCD matrices are equal. Hence we formulate the target loss function as:

$$\min_{tpl, \boldsymbol{L,a,b,c,N}\}} \quad ||M_{p-mts} - M_{t-mts}||^2 \tag{10}$$

We also utilize the Adam gradient descent optimizer to solve the optimization problem. The loss function converged to a value below 0.8, corresponding to a match error of 0.27%.

5 EVALUATION

5.1 Prototype Implementation

5.1.1 Metasurface fabrication. Our tunable metasurface prototype is fabricated using PCB techniques with FPC [22] material as the substrate. The SMV1408 [62] variable capacitor is chosen, capable of tuning capacitance from 4.08 pF to 0.95 pF across a 0 to 30V range, suitable for calibration steps. The unit parameters of the tunable metasurface are as: $g = 0.7$ mm, $w_1 = w_2 = 0.2$ mm, $P = 4$ mm, $H = 2$ mm. Our optimized passive metasurface is fabricated using copper-clad laminate (with FR4 substrate) and etching techniques. The fabricated tunable metasurface and an example of a passive metasurface are shown in Figure 10. The material cost of passive metasurfaces is only around 1 cent, and the active metasurface costs $11.7.

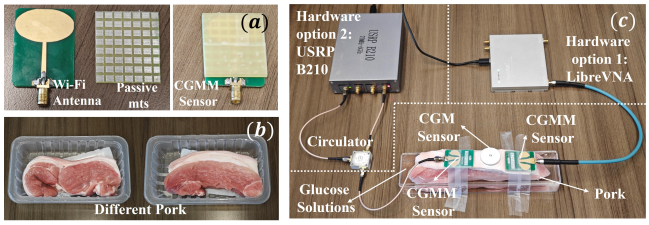

Figure 11: Experimental setup for prototype 1: (a) metasurface affixed to external antennas, (b) selection of varied pork samples for diversity, and (c) pork immersed in glucose solutions to alter tissue fluid glucose levels, with a CGM sensor providing ground truth and VNA/SDR measuring antenna S_{11} parameters

5.1.2 Antenna S_{11} measurement. **Portable radio devices and external antenna.** We select two mainstream portable radio devices to measure the S_{11} parameters of the antenna. One is LibreVNA [74], which is an open source portable VNA and user-friendly. The other is the traditional USRP SDR device, *i.e.*, B210 [56]. When used with a circulator [16], it can also measure the antenna's S_{11} parameters [33]. Specifically, we use the USRP to generate continuous waves at each individual frequency point in the Wi-Fi band and record the corresponding S_{11} parameters. We then performed a frequency sweep to obtain the S_{11} curve across the entire band. This selection allows us to compare the impact of different measurement devices on the glucose sensing accuracy. We use a patch antenna to sense glucose, which can work in the Wi-Fi band. We affix the fabricated passive metasurface onto the antenna, as illustrated in Figure 11(a). The measurement setups of B210 and LibreVNA are shown in Figure 11(c).

Commercial UWB radar module. We use a commercial UWB radar module, the SLMX4 [58], to verify that our proposed metasurface can be easily integrated into existing commercial devices. The SLMX4 supports two UWB bands, 6.0-8.5 GHz and 7.25-10.2 GHz. To obtain the UWB antenna's frequency response shifts to the glucose changes, we initially record the received pulse signals and perform FFT to analyze the frequency response of the TX-RX channel using a perfect corner reflector. Next, we optimize the metasurface for the UWB frequency range, affixed it to the RX antenna, and attach the entire antenna assembly to the test subject, as shown

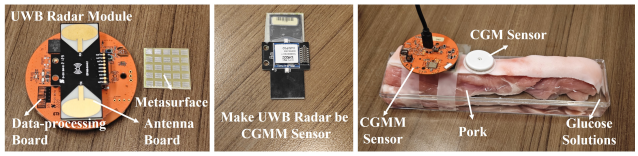

Figure 12: Experimental setup for prototype 2: metasurface affixed to the UWB radar device's RX antenna

(a) Prototype 1: Antenna+VNA (b) Prototype 2: UWB Radar

Figure 13: Setup for human subject experiments

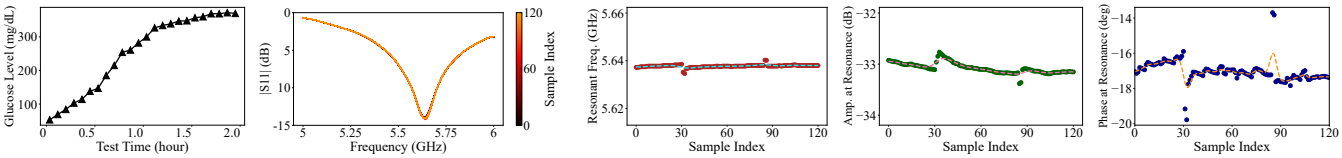

(a) The antenna is directly attached to the pork skin, the pork is immersed in a high-concentration glucose solution for two hours

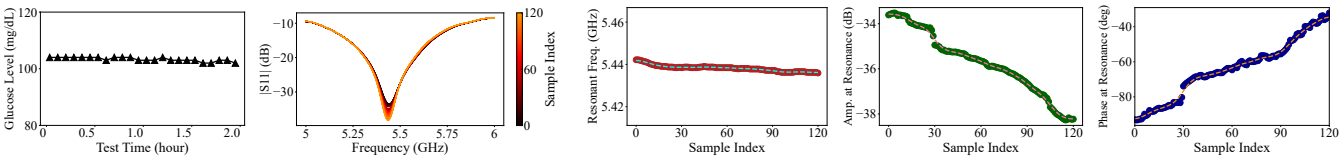

(b) Metasurface affixed to the antenna, which are then attached to the pork skin. The pork is immersed in pure water for two hours

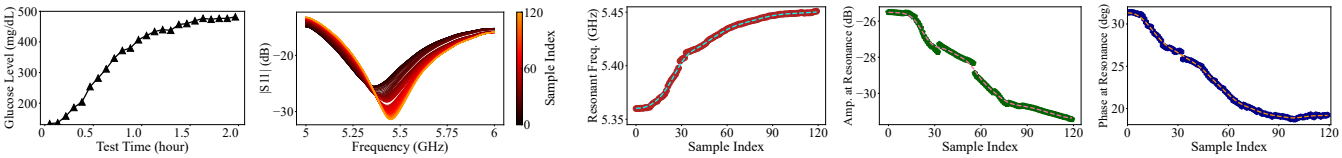

(c) Metasurface affixed to the antenna, which are then attached to the pork skin. The pork is immersed in high-concentration glucose solutions for two hours

Figure 14: Validation of the metasurface's amplification on antenna S_{11} parameter to tissue fluid glucose concentration changes with prototype 1. The first column shows the CGM data. The second column plots the S_{11} parameters, with different colors representing data collected at various time points with an update rate of 1min/sample. The third to fifth columns display the resonance frequency offset, magnitude, and phase variation curves of the S_{11} parameters over time

in Figure 12. Finally, we recalculate the FFT results of the received signals. By comparing these FFT results, we obtain the frequency response of the RX antenna.

5.2 Experiment Setup

5.2.1 Simulation of tissue fluid changes using pork in glucose solutions. For measurements of glucose concentrations in the non-healthy range (200-500 mg/dL), we utilize pork as the experimental subject. Pork is immersed in high-concentration glucose solutions, allowing glucose molecules to diffuse into the tissue fluid over time, thereby increasing the glucose concentration within the pork. A Libre Freestyle CGM sensor [41] is insetherted into the pork to obtain ground truth measurements. Subsequently, two types of prototype CGMM sensors are affixed to the surface of the pork skin to measure the S_{11} parameters of the antenna. Additionally, we employ a tunable metasurface for calibration across different pork samples, taking into account the varying parameters of skin, fat, and muscle. The specific setups are illustrated in Figure 11 and Figure 12.

5.2.2 Human subject experiment. To evaluate the effectiveness of our CGMM sensor in measuring human glucose levels, we utilize 3D printing technology to create a mounting bracket for the metasurface and antenna. The bracket can be integrated into the wrist band, enhancing wearability and ensuring secure contact between the metasurface and the human skin. During the test, volunteers are required to drink high-glucose beverages to induce glucose fluctuations. We also let volunteers wear a Libre Freestyle CGM sensor to record the ground truth. The specific setup is illustrated in Figure 13.

5.3 Performance in Pork-based Experiments

5.3.1 Effectiveness of the optimized metasurface. We conduct three experiments with CGMM prototype 1 (with LibreVNA) to validate the effectiveness of the designed metasurface, with results shown in Figure 14. Each pork experiment

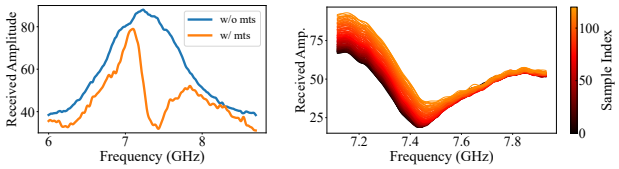

(a) FFT of received pulse (b) FFT results over the time index

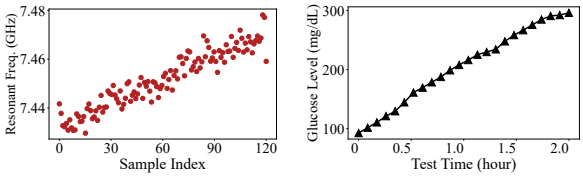

(c) Resonatance freq. shift (d) CGM measurment data

Figure 15: Results of prototype 2 in pork experiments confirm that the metasurface amplifies the UWB radar's frequency response to glucose concentration changes

lasts only 2 hours at a constant room temperature of 26°C to ensure the pork remained fresh. We find the following: (a) With only the antenna, glucose changes have negligible effect on the S_{11} parameters. (b) With the metasurface, the S_{11} parameter exhibits strong resonance. At constant glucose levels, there is minimal resonance frequency shift but some variation in resonance amplitude and phase. (c) As glucose concentration increases, the S_{11} parameter frequency shifts closely track the glucose changes, while amplitude and phase changes are less consistent. We also conduct one experiments with CGMM prototype 2 (with 6-8.5 GHz band), with results shown in Figure 15. We observe that FFT analysis of the received signals from UWB RX antenna shows effective resonance with the added metasurface. The resonance frequency shifts right consistently as glucose concentration increases, confirming the metasurface's effectiveness in the UWB frequency band.

The resonance frequency shifts from the measurements linearly correlate with glucose concentration changes, allowing direct conversion between the two. For example, in Figure 14(c), given the S_{11} parameter at time point index i with a resonance frequency f_i (*i.e.*, $argmin(|S_{11}|)$), the glucose concentration can be calculated as: $\frac{f_i - f_1}{K}$, where f_1 is the resonance frequency from the first measurement and K is a conversion constant. In this case, we set it to $0.23\frac{MHz}{mg/dL}$.

5.3.2 Performance analysis of prototype 1. We conduct five experiments, each using a new piece of pork immersed in glucose solutions. In each experiment, we use the tunable metasurface for calibration and obtain a practically optimized passive metasurface for the target pork. The testing setups are shown in Figure 11, and the recorded S_{11} parameters are smoothed for the post-processing and visualization. We convert the resonance frequency shift into the relative changes

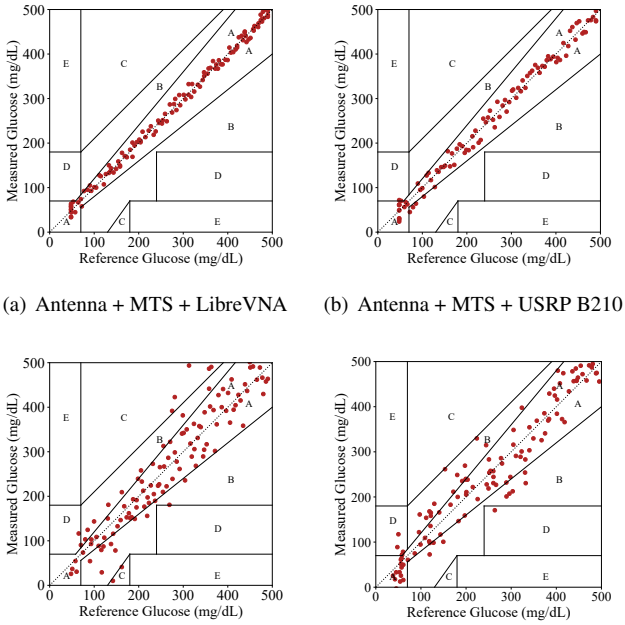

(a) Antenna + MTS + LibreVNA (b) Antenna + MTS + USRP B210

(c) UWB band: 6-8.5 GHz (d) UWB band: 7.25-10.2 GHz

Figure 16: Clarke error analysis for prototype 1&2 in pork experiments. (a) Region A-E probabilities: 100%, 0, 0, 0, 0. (b) Region A-E: 95.8%, 4.2%, 0, 0, 0. (c) Region A-E: 66.7%, 26.7%, 4.2%, 2.5%, 0. (d) Region A-E: 70.6%, 22.5%, 0.8%, 6.1%, 0[1]

in glucose concentration. For absolute glucose concentration error analysis, we use the CGM data from the first time point as a reference and add it to the CGMM measurements.

We use Clark error analysis[1] to evaluate the measurement error between our CGMM system and the CGM sensor. The results, shown in Figure 16(a) and (b), indicate a high similarity between the CGMM system and CGM measurements under pork experiments. The performance of the B210 is slightly inferior to the LibreVNA, likely due to the circulator's less effective signal isolation. High-quality signal-isolating circulators are expensive and would significantly increase the cost of a CGMM prototype. To address this, we propose replacing single-antenna S_{11} measurements with two antennas to measure the channel parameters between them. Fundamentally, both methods reflect the same principle: the channel characteristics induced by electromagnetic waves as they pass through the metasurface, skin, fat, muscle, and other tissues. This design eliminates the need for costly circulators, making

[1]The Clark grid [10] divides the scatterplot of the reference and evaluation glucose meters into five regions: Region A includes values within 20% of the reference. Region B contains points outside of this range that would not lead to inappropriate treatment. Region C includes points that could lead to unnecessary treatment. Region D contains points indicating a potentially dangerous failure to detect hypo- or hyperglycemia. Region E consists of points that could confuse the treatment of hypo- and hyperglycemia.

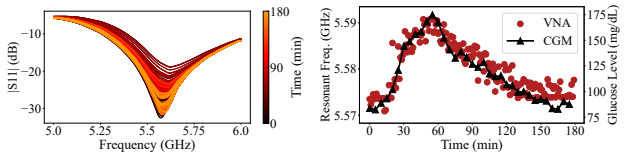

(a) S_{11} curves over time (b) Resonance Freq. vs. CGM results

Figure 17: Exemplar results of prototype 1 (with LibreVNA) in human subject experiments

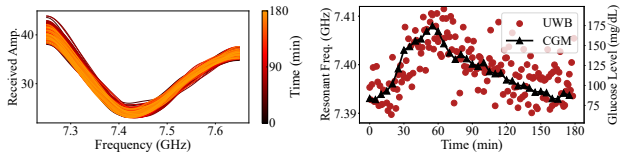

(a) FFT results over time (b) Resonance Freq. vs. CGM results

Figure 18: Exemplar results of prototype 2 (UWB band: 6-8.5 GHz) in human subject experiments

the system more practical and cost-effective. In the prototype based on commercial UWB radar, we validate the feasibility of using two antennas to measure equivalent S_{11} parameters.

5.3.3 Performance analysis of prototype 2. We configure the UWB radar to operate in two frequency bands and optimize the passive metasurface for different pork samples, repeating each experiment five times. The SLMX4 board's frequency domain resolution is 388.8 MHz. To improve the identification of peak positions, we zero-pad the original sampling data to 32,768 points for FFT analysis, which enhances computational resolution and yields smoother signals without increasing physical resolution. Clarke error analysis is employed to evaluate the performance of Prototype 2, as shown in Figure 16 (c) and (d). Compared to Prototype 1, Prototype 2 demonstrate lower measurement accuracy, primarily due to its limited frequency resolution. However, the resonance points from the frequency response curve remains strongly correlated with glucose changes.

5.4 Performance in Human Experiments

We recruit ten volunteers to test the performance of our system, including 8 males and 2 females, aged 22 to 48; these volunteers are healthy and do not have diabetes[2]. During the test, we ask the volunteers to drink two cups of high-sugar beverages (a total of around 800 mL) and conduct measurements over a 3-hour period. We install two CGMM prototypes on each of the volunteers' arms, as shown in Figure 13. Throughout the test, the volunteers are seated and only slight arm movements are allowed. For each volunteer, we need a calibration for obtaining the value of K. We measure an

[2]Our human subject experiments have received IRB approval from the Department of Computer Science and Technology at Tsinghua University.

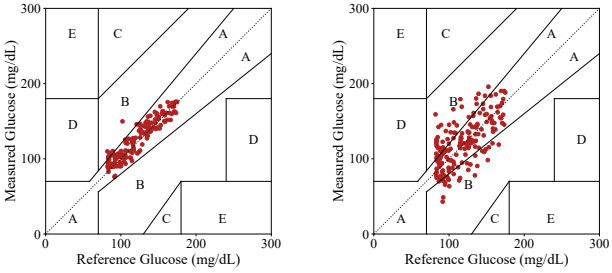

(a) Antenna+LibreVNA (b) UWB Radar (6-8.5GHz)

Figure 19: Clarke error analysis for in human subject experiments. (a) Region A-E probabilities: 94.4%, 5.6%, 0, 0, 0. (b) Region A-E: 63.8%, 36.2%, 0, 0, 0[1]

increase in blood glucose levels three times (*e.g.*, following the intake of a glucose solution) and compare the resonance frequency point obtained from the CGMM prototype with the ground truth recorded by the CGM sensor. From these three calibration measurements, we calculate the average value of K, which is then used to convert resonance frequency shift parameters into changes in blood glucose levels in the CGMM.

Figure 17 and Figure 18 display an exemplar collected data for the participant 1. We find that both CGMM prototypes performed well in real-world human subject testing scenarios. From the Clarke Error Grid analysis (see Figure 19), we find that 88.3% and 63.8% of the measurements from prototype 1 and 2, respectively, fall within Region A, which is considered accurate enough for making correct clinical decisions. Meanwhile, 11.7% and 36.2% of the measurements from Prototype 1 and 2 fall within Region B. Region B does not lead to inappropriate treatment. Collectively, 100% measurements lead to appropriate treatement using both prototypes.

Results of the relative difference analysis of the human subject experiments are shown in Figure 20. The prototype 1 with the LibreVNA provides the most accurate measurements, with relative errors ranging from -5.02% (the first quartile) to 6.93% (the third quartile), and RMSE is 9.65 mg/dL. The black markers in Figure 20 indicate the singularity points, which may be caused by factors such as device measurement noise and significant movements of the participant's arm. The UWB radar module (prototype 2) operating in the frequency band of 7.25-10.2 GHz, constrained by its limited sampling points, also shows the satisfied accuracy, with relative errors ranging from -13.76% (the first quartile) to 15.95% (the third quartile), and RMSE is 20.54 mg/dL.

Timing tests on passive metasurfaces. We conduct timeliness experiments on calibrated passive metasurfaces and the K value, involving three participants (ID 1-3). Specifically, we use metasurfaces calibrated for each participant three months earlier and test their performance. The experimental results are shown in Figure 21. We compare the accuracy

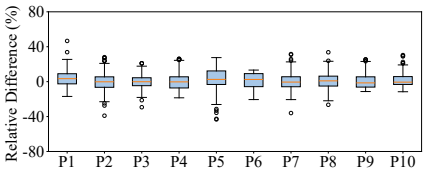

(a) Prototype with LibreVNA

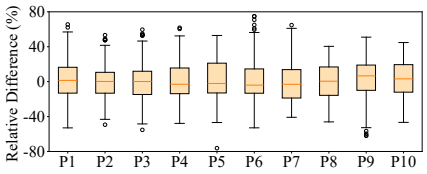

(b) Prototype with UWB (7.25-10.2GHz)

Figure 20: Relative difference bar plots of predicted glucose levels by CGMM compared to the ground truth collected by the CGM sensors. P1-10 refer to Participants 1-10

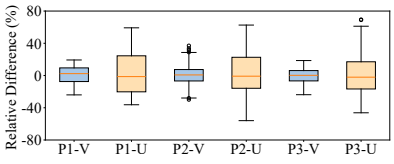

Figure 21: Relative difference bar plots with the calibrated passive metasurfaces and K values 3 months ago. V and U mean VNA and UWB

of the current experiments with the experiments conducted three months earlier (see P1-3 in Figure 20). Prototype 1, equipped with the LibreVNA, provides glucose monitoring performance with relative errors ranging from -6.96% (the first quartile) to 7.68% (the third quartile), and an RMSE of 11.82 mg/dL. While, prototype 2, equipped with the UWB radar device, demonstrates performance with relative errors ranging from -17.58% (the first quartile) to 21.39% (the third quartile), and an RMSE of 324.90 mg/dL. The experimental results show that metasurfaces and K values calibrated three months ago can still detect blood glucose level changes, though with slightly reduced accuracy.

6 DISCUSSION

Fusion of relevant sensors for compensation. The experiment results of the CGMM on pork are superior to those from human experiments. This discrepancy may be attributed to slight arm movements during the experiments, which affected the RF cable. Changes in the RF cable can lead to variations in its effective capacitance and other parameters, resulting in errors in the CGMM system's resonance point measurements. Additionally, the humidity and temperature of the human's tissues can cause slight variations in the permittivity changes of skin, fat, and muscle, and cause the singularity point in Figure 20. In future work, we will address these influences by integrating data from relevant sensors.

Effect of other components on the tissue permittivity. The permittivity of blood is easily affected by factors such as blood glucose and lipids [49], making it unreliable for accurately estimating blood glucose levels. Glucose molecules, being small, can achieve equilibrium between blood and tissue fluid through osmotic balance when glucose levels change [20]. The permittivity of tissue fluid may also be affected by variations in other small-molecule components. However, the changes of other components are much smaller: glucose concentration may change from 30 mg/dL to 400 mg/dL for diabetic patients. While sodium and chloride levels, despite being present in significant amounts, change by a much smaller amount: sodium changes from 310 mg/dL to 333 mg/dL, and chloride changes from 337 mg/dL to 372 mg/dL [40]. Other minerals have even smaller concentrations in blood, such as magnesium (1.8-3.4 mg/dL), calcium (8.5-10.5 mg/dL), and potassium (13.6-21.4 mg/dL). Thus, we assume changes in other components have negligible impact on blood permittivity, following prior studies [9, 65, 67].

Absolute glucose level and error of CGMM. Non-invasive measurement methods require an initial accurate calibration of absolute blood glucose levels. A common approach involves using invasive techniques to measure a user's fasting blood glucose for calibration, followed by utilizing non-invasive methods for ongoing monitoring of glucose concentration changes. The non-invasive measurement technique we propose may not achieve the same high level of accuracy as invasive methods. However, the ability to accurately detect abnormal events such as hypoglycemia and hyperglycemia is still of significant importance for individuals with diabetes.

7 CONCLUSION

We present CGMM, a system for non-invasive glucose sensing in wearable devices through the innovative integration of metasurfaces. We validate the system's performance through human subject experiments, demonstrating its effectiveness. Building on these promising results, we plan to conduct more extensive user studies and refine our system, paving the way for its deployment in daily applications.

ACKNOWLEDGMENTS

We thank the anonymous reviewers for their constructive comments. This work is supported in part by NSFC (No. 62432004 and 62072306) and by a grant from the Guoqiang Institute, Tsinghua University.

REFERENCES

[1] Adil. Cgm's and skin reactions – the definitive guide. https://notjustapatch.com/cgm-skin-irritation/, 2024.

[2] J. A. Al-Lawati. Diabetes mellitus: a local and global public health emergency! *Oman medical journal*, 32(3):177, 2017.

[3] Ansys. Ansys hfss best-in-class 3d high frequency structure simulation software. https://www.ansys.com/zh-cn/products/electronics/ansys-hfss, 2023.

[4] A. Bauer, O. Hertzberg, A. Küderle, D. Strobel, M. A. Pleitez, and W. Mäntele. Ir-spectroscopy of skin in vivo: Optimal skin sites and

properties for non-invasive glucose measurement by photoacoustic and photothermal spectroscopy. *Journal of biophotonics*, 11, 2018.

[5] M. R. Burge, S. Mitchell, A. Sawyer, and D. S. Schade. Continuous glucose monitoring: the future of diabetes management. *Diabetes Spectrum*, 21(2):112–119, 2008.

[6] G. Cappon, M. Vettoretti, G. Sparacino, and A. Facchinetti. Continuous glucose monitoring sensors for diabetes management: a review of technologies and applications. *Diabetes & metabolism journal*, 43(4):383–397, 2019.

[7] God! this watch can measure the blood sugar value in a towel? https://news.cctv.com/2024/12/27/ARTInRBvwQurvRM2U948JmBm241227.shtml.

[8] What is a continuous glucose monitor (cgm)? https://payer.freestyle.abbott/us-en/Resources/what-is-cgm.html.

[9] E. L. Chuma, Y. Iano, G. Fontgalland, and L. L. B. Roger. Microwave sensor for liquid dielectric characterization based on metamaterial complementary split ring resonator. *IEEE Sensors Journal*, 18(24):9978–9983, 2018.

[10] Clarke error grid. https://en.wikipedia.org/wiki/Clarke_Error_GridClarkeErrorGrid.

[11] J. Clover. Apple watch blood glucose team gains new lead. https://www.macrumors.com/2023/09/14/apple-watch-blood-glucose-team-update/, 2023.

[12] CONGA. Cog - hybrid glucometer: Meet the world's first hybrid, non-invasive glucometer. https://www.cnogacare.co/cog-hybrid-glucometer, 2023.

[13] S. Delbeck, T. Vahlsing, S. Leonhardt, G. Steiner, and H. M. Heise. Non-invasive monitoring of blood glucose using optical methods for skin spectroscopy—opportunities and recent advances. *Analytical and bioanalytical chemistry*, 411:63–77, 2019.

[14] A. Dhekne, M. Gowda, Y. Zhao, H. Hassanieh, and R. R. Choudhury. Liquid: A wireless liquid identifier. In *Proceedings of the 16th annual international conference on mobile systems, applications, and services*, pages 442–454, 2018.

[15] D1 health smart watch non-invasive glucose detection smart watch. https://dynasynq.com/products/dynasynq-d1-health-smart-watch-non-invasive-glucose-detection.

[16] ebay. 1pcs new for cs-3060s 3000-6000mhz 3-6ghz sma 100w circulator. https://www.ebay.co.uk/itm/374636346764, 2024.

[17] A. Ebrahimi, J. Scott, and K. Ghorbani. Microwave reflective biosensor for glucose level detection in aqueous solutions. *Sensors and Actuators A: Physical*, 301:111662, 2020.

[18] Do not use smartwatches or smart rings to measure blood glucose levels: Fda safety communication. https://www.fda.gov/medical-devices/safety-communications/do-not-use-smartwatches-or-smart-rings-measure-blood-glucose-levels-fda-safety-communication.

[19] C. Feng, J. Xiong, L. Chang, J. Wang, X. Chen, D. Fang, and Z. Tang. Wimi: Target material identification with commodity wi-fi devices. In *2019 IEEE 39th International Conference on Distributed Computing Systems (ICDCS)*, pages 700–710. IEEE, 2019.

[20] K. Fiedorova, M. Augustynek, J. Kubicek, P. Kudrna, and D. Bibbo. Review of present method of glucose from human blood and body fluids assessment. *Biosensors and Bioelectronics*, 211:114348, 2022.

[21] I. foundation. Tissue properties. https://itis.swiss/virtual-population/tissue-properties/database/dielectric-properties, 2023.

[22] Fpc. https://www.nexpcb.com/blog/an-introduction-to-fpc-materials.

[23] S. Gabriel, R. Lau, and C. Gabriel. The dielectric properties of biological tissues: Iii. parametric models for the dielectric spectrum of tissues. *Physics in medicine & biology*, 41(11):2271, 1996.

[24] Samsung hints that an optical blood glucose sensor might be closer than we think. https://www.gsmarena.com/samsung_hints_that_an_optical_blood_glucose_sensor_might_be_closer_than_we_think-news-66262.php.

[25] R. Gulich, M. Köhler, P. Lunkenheimer, and A. Loidl. Dielectric spectroscopy on aqueous electrolytic solutions. *Radiation and environmental biophysics*, 48:107–114, 2009.

[26] L. Gun, D. Ning, and Z. Liang. Effective permittivity of biological tissue: comparison of theoretical model and experiment. *Mathematical Problems in Engineering*, 2017(1):7249672, 2017.

[27] U. Ha, J. Leng, A. Khaddaj, and F. Adib. Food and liquid sensing in practical environments using rfids. In *Proceedings of the 17th USENIX Symposium on Networked Systems Design and Implementation (NSDI'20)*, 2020.

[28] U. Ha, Y. Ma, Z. Zhong, T.-M. Hsu, and F. Adib. Learning food quality and safety from wireless stickers. In *Proceedings of the 17th ACM workshop on hot topics in networks*, pages 106–112, 2018.

[29] J. Hanna, Y. Tawk, S. Azar, A. H. Ramadan, B. Dia, E. Shamieh, S. Zoghbi, R. Kanj, J. Costantine, and A. A. Eid. Wearable flexible body matched electromagnetic sensors for personalized non-invasive glucose monitoring. *Scientific Reports*, 12(1):14885, 2022.

[30] T. Harris. Best glucose meters to monitor your blood sugar in 2023. https://www.forbes.com/health/conditions/diabetes/best-glucose-meters/, 2023.

[31] J. Huang, Y. Zhang, and J. Wu. Review of non-invasive continuous glucose monitoring based on impedance spectroscopy. *Sensors and Actuators A: Physical*, 311:112103, 2020.

[32] X. Huang, C. Leduc, Y. Ravussin, S. Li, E. Davis, B. Song, Q. Wang, D. Accili, R. Leibel, and Q. Lin. Continuous monitoring of glucose in subcutaneous tissue using microfabricated differential affinity sensors. *Journal of diabetes science and technology*, 6(6):1436–1444, 2012.

[33] A. Hussain, A. A. Glazunov, B. Þ. Einarsson, and P.-S. Kildal. Antenna measurements in reverberation chamber using usrp. *IEEE Transactions on Antennas and Propagation*, 64(3):1152–1157, 2016.

[34] T. T. Islam, M. S. Ahmed, M. Hassanuzzaman, S. A. Bin Amir, and T. Rahman. Blood glucose level regression for smartphone ppg signals using machine learning. *Applied Sciences*, 11(2):618, 2021.

[35] ISRAEL21C. Test your glucose level without drawing blood. https://www.israel21c.org/test-your-glucose-level-without-drawing-blood/, 2023.

[36] T. Karacolak, E. C. Moreland, and E. Topsakal. Cole–cole model for glucose-dependent dielectric properties of blood plasma for continuous glucose monitoring. *Microwave and Optical Technology Letters*, 55(5):1160–1164, 2013.

[37] L. Kennedy. Finger-stick glucose monitoring. https://www.ncbi.nlm.nih.gov/pmc/articles/PMC2845057/, 2023.

[38] S. Kim, J. Malik, J. M. Seo, Y. M. Cho, and F. Bien. Subcutaneously implantable electromagnetic biosensor system for continuous glucose monitoring. *Scientific Reports*, 12(1):17395, 2022.

[39] T. Li, D. Bai, T. Prioleau, N. Bui, T. Vu, and X. Zhou. Noninvasive glucose monitoring using polarized light. In *Proceedings of the 18th conference on embedded networked sensor systems*, pages 544–557, 2020.

[40] T. H. S. Library. University of michigan library. https://www.lib.umich.edu/locations-and-hours/taubman-health-sciences-library, 2023.

[41] Freestyle libre. trusted by 4 million users worldwide. https://freestylelibre.com.

[42] A. Liu, G. Li, W. Yan, and L. Lin. Combined effects of ppg preprocess and dynamic spectrum extraction on predictive performance of non-invasive detection of blood components based on dynamic spectrum. *Infrared Physics & Technology*, 92:436–442, 2018.

[43] R. Ma and W. Hu. Rf-mediator: Tuning medium interfaces with flexible metasurfaces. In *Proceedings of the 30th Annual International Conference on Mobile Computing and Networking*, pages 155–169, 2024.

[44] R. Ma, S. Zheng, H. Pan, L. Qiu, X. Chen, L. Liu, Y. Liu, W. Hu, and J. Ren. Automs: Automated service for mmwave coverage optimization using low-cost metasurfaces. In *Proceedings of the 30th Annual International Conference on Mobile Computing and Networking*, pages 62–76, 2024.

[45] macrumors. Apple Watch Blood Glucose Monitoring Likely Still 'Three to Seven Years' Away. https://www.macrumors.com/2023/03/26/apple-watch-blood-glucose-up-to-seven-years-away/, 2023.

[46] E. Moser, L. Crew, and S. Garg. Role of continuous glucose monitoring in diabetes management. *Avances en Diabetología*, 26(2):73–78, 2010.

[47] M. Naresh, V. S. Nagaraju, S. Kollem, J. Kumar, and S. Peddakrishna. Non-invasive glucose prediction and classification using nir technology with machine learning. *Heliyon*, 10(7), 2024.

[48] H. news. Non-invasive device could end daily finger pricking for people with diabetes. https://www.leeds.ac.uk/news/article/3723/, 2023.

[49] A. K. Nilsson, U. Sjöbom, K. Christenson, and A. Hellström. Lipid profiling of suction blister fluid: comparison of lipids in interstitial fluid and plasma. *Lipids in health and disease*, 18:1–11, 2019.

[50] N. I. of Diabetes, Digestive, and K. Diseases. Continuous glucose monitoring. https://www.niddk.nih.gov/health-information/diabetes/overview/managing-diabetes/continuous-glucose-monitoring, 2023.

[51] A. E. Omer, S. Safavi-Naeini, R. Hughson, and G. Shaker. Blood glucose level monitoring using an fmcw millimeter-wave radar sensor. *Remote Sensing*, 12(3):385, 2020.

[52] A. E. Omer, G. Shaker, S. Safavi-Naeini, H. Kokabi, G. Alquié, F. Deshours, and R. M. Shubair. Low-cost portable microwave sensor for non-invasive monitoring of blood glucose level: Novel design utilizing a four-cell csrr hexagonal configuration. *Scientific Reports*, 10(1):15200, 2020.

[53] H. Pan, L. Qiu, B. Ouyang, S. Zheng, Y. Zhang, Y.-C. Chen, and G. Xue. Pmsat: Optimizing passive metasurface for low earth orbit satellite communication. In *Proceedings of the 29th Annual International Conference on Mobile Computing and Networking*, pages 1–15, 2023.

[54] D. M. Pozar. *Microwave Engineering (4th Edition)*. John Wiley & Sons, Inc., 2011.

[55] R. G. Priyadarshini, M. Kalimuthu, S. Nikesh, and M. Bhuvaneshwari. Review of ppg signal using machine learning algorithms for blood pressure and glucose estimation. In *IOP conference series: materials science and engineering*, volume 1084, page 012031. IOP Publishing, 2021.

[56] E. Research. Usrp b210 sdr kit - dual channel transceiver (70 mhz - 6ghz) - ettus research. https://www.ettus.com/all-products/ub210-kit/, 2024.

[57] K. Sasaki, K. Wake, and S. Watanabe. Development of best fit cole-cole parameters for measurement data from biological tissues and organs between 1 mhz and 20 ghz. *Radio science*, 49(7):459–472, 2014.

[58] SensorLogic. Slmx4 uwb radar module. https://sensorlogic.ai/sensor-products/SLMX4, 2024.

[59] G. Shaker, K. Smith, A. E. Omer, S. Liu, C. Csech, U. Wadhwa, S. Safavi-Naeini, and R. Hughson. Non-invasive monitoring of glucose level changes utilizing a mm-wave radar system. *International Journal of Mobile Human Computer Interaction (IJMHCI)*, 10(3):10–29, 2018.

[60] C. Shan, H. Yang, J. Song, D. Han, A. Ivaska, and L. Niu. Direct electrochemistry of glucose oxidase and biosensing for glucose based on graphene. *Analytical chemistry*, 81(6):2378–2382, 2009.

[61] F. Shang, P. Yang, Y. Yan, and X.-Y. Li. Liqray: non-invasive and fine-grained liquid recognition system. In *Proceedings of the 28th Annual International Conference on Mobile Computing And Networking*, pages 296–309, 2022.

[62] Smv1408. https://www.skyworksinc.com/Products/Diodes/SMV1408-Series.

[63] C. Song, W.-H. Fan, L. Ding, X. Chen, Z.-Y. Chen, and K. Wang. Terahertz and infrared characteristic absorption spectra of aqueous glucose and fructose solutions. *Scientific Reports*, 8(1):8964, 2018.

[64] Y. Song, H. Pan, L. Ge, L. Qiu, S. Kumar, and Y.-C. Chen. Microsurf: Guiding energy distribution inside microwave oven with metasurfaces. In *Proceedings of the 30th Annual International Conference on Mobile Computing and Networking*, pages 1346–1360, 2024.

[65] E. Topsakal, T. Karacolak, and E. C. Moreland. Glucose-dependent dielectric properties of blood plasma. In *2011 XXXth URSI General assembly and scientific symposium*, pages 1–4. IEEE, 2011.

[66] T. Torii, H. Chiba, T. Tanabe, and Y. Oyama. Measurements of glucose concentration in aqueous solutions using reflected thz radiation for applications to a novel sub-thz radiation non-invasive blood sugar measurement method. *Digital health*, 3:2055207617729534, 2017.

[67] V. Turgul and I. Kale. Characterization of the complex permittivity of glucose/water solutions for noninvasive rf/microwave blood glucose sensing. In *2016 IEEE International Instrumentation and Measurement Technology Conference Proceedings*, pages 1–5. IEEE, 2016.

[68] Y. Wang, H. Pan, L. Qiu, L. Zhong, J. Liu, R. Ma, Y.-C. Chen, G. Xue, and J. Ren. Gpms: Enabling indoor gnss positioning using passive metasurfaces. In *Proceedings of the 30th Annual International Conference on Mobile Computing and Networking*, pages 1424–1438, 2024.

[69] Effective medium approximations. https://en.wikipedia.org/wiki/Effective_medium_approximations.

[70] B. Xie, J. Xiong, X. Chen, E. Chai, L. Li, Z. Tang, and D. Fang. Tagtag: material sensing with commodity rfid. In *Proceedings of the 17th conference on embedded networked sensor systems*, pages 338–350, 2019.

[71] J. Yadav, A. Rani, V. Singh, and B. M. Murari. Prospects and limitations of non-invasive blood glucose monitoring using near-infrared spectroscopy. *Biomedical signal processing and control*, 18:214–227, 2015.

[72] Optical sensing solution for an accessible, non-invasive continuous blood glucose monitor (nigm). https://ventures.yale.edu/yale-technologies/optical-sensing-solution-accessible-non-invasive-continuous-blood-glucose-monitor.

[73] J. Yang, L. Qi, B. Li, L. Wu, D. Shi, J. A. Uqaili, and X. Tao. A terahertz metamaterial sensor used for distinguishing glucose concentration. *Results in Physics*, 26:104332, 2021.

[74] Zeenko. Librevna. https://www.zeenko.tech/librevna, 2024.

[75] G. Zhang, Z. Mei, Y. Zhang, X. Ma, B. Lo, D. Chen, and Y. Zhang. A noninvasive blood glucose monitoring system based on smartphone ppg signal processing and machine learning. *IEEE Transactions on Industrial Informatics*, 16(11):7209–7218, 2020.

[76] Y. Zhang, L. Zhang, L. Wang, S. Shao, B. Tao, C. Hu, Y. Chen, Y. Shen, X. Zhang, S. Pan, et al. Subcutaneous depth-selective spectral imaging with mμsors enables noninvasive glucose monitoring. *Nature Metabolism*, pages 1–13, 2025.

APPENDIX

A PARAMETERS OF THE COLE-COLE MODEL

Conc. (mg/dL)	0	100	200	300	400	500
ϵ_S	79.15	79.06	78.92	78.86	78.82	78.78
ϵ_∞	9.99	10.03	10.14	10.48	10.96	11.27
$\tau(1e^{-12})$	9.26	9.24	9.22	9.28	9.36	9.42

Table 1: Parameters of the single pole Cole-Cole model for five different concentrations of glucose solutions

Conc. (mg/dL)	0	100	200	300	400	500
ϵ_∞	2.32	2.31	2.29	2.72	2.98	2.97
$\sigma_{DC}\ (S/m)$	0.0222	0.018	0.010	0.010	0.010	0.010
$\tau_1\ (1e^{-12})$	7.87	7.07	5.76	7.48	10.56	14.39
$\epsilon_{s,1} - \epsilon_{\infty,1}\ (\Delta_1)$	2.14	2.1	2.0	1.5	1.3	1.5
α_1	0.002	0.001	0.001	0.047	0.154	0.273
$\tau_2\ (1e^{-8})$	1.93	1.85	1.34	1.81	1.06	1.30
$\epsilon_{s,2} - \epsilon_{\infty,2}\ (\Delta_2)$	19.7	26	31	40	31	45
α_2	0.259	0.22	0.163	0.157	0.087	0.001

Table 2: Parameters of the Cole-Cole models for five different glucose concentrations of fat tissue

Conc. (mg/dL)	0	100	200	300	400	500
ϵ_∞	4.32	4.24	4.24	5.00	4.83	4.62
$\sigma_{DC}\ (S/m)$	0.354	0.362	0.310	0.376	0.397	0.390
$\tau_1\ (1e^{-12})$	1.040	1.034	1.034	1.056	1.061	1.061
$\epsilon_{s,1} - \epsilon_{\infty,1}\ (\Delta_1)$	59.3	59.4	59.3	58.4	58.8	59.2
α_1	0.240	0.243	0.246	0.242	0.248	0.252
$\tau_2\ (1e^{-7})$	9.10	8.98	7.96	9.28	9.37	9.20
$\epsilon_{s,2} - \epsilon_{\infty,2}\ (\Delta_2)$	23500	22977	25000	22146	21982	22214
α_2	0.093	0.092	0.080	0.097	0.091	0.088

Table 3: Parameters of the Cole-Cole models for five different glucose concentrations of muscle tissue